Experimental and numerical investigation of heat transfer in an array of impingement jets on a concave surface

B. Yang[a], S. Chang[a, *], H. Wu[b, **], Y. Zhao[a], M. Leng[a]

[a]*School of Aeronautics Science and Engineering, Beihang University, Beijing 100183, China*

[b]*School of Engineering and Technology, University of Hertfordshire, Hatfield, AL10 9AB, United Kingdom*

[*]Corresponding author. Tel.: +86 010 8233 8008, *E-mail address:* sn_chang@buaa.edu.cn (Chang Shinan)

[**]Corresponding author. Tel.: +44 (0)1707 284265, Fax: +44 (0)1707 285086,

E-mail address: h.wu6@herts.ac.uk (Hongwei Wu)

Abstract:

In this article, a combined experimental and computational study was conducted to investigate the heat transfer characteristics of sonic impingement jets on the concave surface of the leading edge of a NACA0015 airfoil. Both the local/average Nusselt number ($Nu / \overline{Nu}$) distributions and flow pattern in the impingement region were obtained for H/d ranging from 10 to 25, S/d from 20 to 35, and d from 2 to 5 mm, and the jet inclination angle (θ) varied from 0° to 30°. The suitability of eight different turbulence models were investigated and verified. Streamlines and velocity distributions around the stagnation point were also obtained by numerical calculation. Comparison between the numerical work and the experimental results indicated that (1) both Nu and $\overline{Nu}$ were enhanced with H/d=10, S/d=30, and θ=15° in the current study. The impinging multi-jet heat transfer capacity could be augmented if the appropriate structure variables are determined, and (2) enlarging the diameters of the jets holes (d) could not significantly improve the heat transfer performance in the anti-icing system of aircraft.

Keywords: heat transfer; impingement; concave surface, leading edge, turbulence model.

Nomenclature

A = total surface area, mm^2

d = diameter of the jet hole, mm

D = diameter of the tube, mm

D_w = cross-diffusion term

$\vec{F}$ = external body forces, N

G_k = turbulence kinetic energy, m^2/s^2

G_θ = generation of ω

h = convective heat coefficient, W/m^2·K

H/d = dimensionless distance between the jets and the stagnation point

$\vec{J}$ = diffusion flux, kg/(m^2·s^{-1})

k_{eff} = effective conductivity, W/m·K

l = characteristic length, mm

Nu = Nusselt number

$\overline{Nu}$ = average Nusselt number

n = number of thermocouples

p = static pressure, pa

q_{heat} = heating flux, W/m^2

q_{conv} = effective heat flux, W/m^2

q_{loss} = heat flux loss, W/m^2

R = resistance of the electro - thermal wire, Ω

Re = Reynolds number

S_k, S_w = source terms

S/d = dimensionless distance between the adjacent jets

T_w = wall temperature, °C

T_f = jet air temperature, °C

V = voltage for heating, Volt

y^+ = dimensionless height of the first layer cells near the wall

$\overline{y^+}$ = average value of y^+

Y_k = dissipation of k

Y_ω = dissipation of ω

Greek symbols

ω = specific dissipation rate

θ = jet inclination angle, °

$\overline{\overline{\tau}}$ = stress tensor

$\rho\vec{g}$ = gravitational body force, N

Γ_k = effective diffusivity of k

Γ_ω = effective diffusivity of ω

ν = kinematic viscosity, m^2/s

ε = turbulent dissipation rate, m^2/s^3

1. Introduction

The use of an impingement jet is an effective method to enhance the heat transfer process since the heat transfer coefficient is much higher in the stagnation point than that in the forced convection flows. Impingement is not new in concept but has still been widely used in many practical applications, such as hot-air anti-icing system on the aircraft [1-2], gas turbine blade [3], electronic components [4]. Heat transfer in the impinging jets has been extensively studied to provide better heat transfer performance on the solid walls as a means of improving the system design.

Compared with the single jet, the multi-jet approach [5] has the special fountain flow region due to the expansion of the shear layer between two jets, resulting in an enhanced technology for providing more uniform heating or cooling [6]. The heat and mass transfer of multi-jet impingement are very complex due to many control factors such as structure parameters i.e., impingement wall structure, holes structure and flow parameters i.e., Re, cross flow, jet fluid type [7]. Many studies were mainly focused on the structure parameters of the multi-jet impingement. Changing the surface structure of the impinging wall could increase the heat transfer efficiency. The particles of the roughened wall at the micron level mainly affects the thickness of the boundary layer region, whereas the larger miniature protrusions of roughened surface affects the velocity and turbulence distributions at both the entire boundary layer and the fully turbulent region [8, 9]. The fluid types can have a great influence on the heat transfer coefficient of a fluid–solid impingement jet [10].

A quite number of research results show that changing the hole shape can be used as an effective passive control technique for heat transfer enhancement of an impingement jet. Lee [11] and Brignoni [12] found that the sharp-edged nozzle jet yields higher heat transfer rates than either the standard-edged or square-edged nozzle jets in the impingement stagnation region. Furthermore, the studies of Ianiro and Cardone [13] and Wannassi and Monnoyer [14] showed that the fountain flow intensity of multi-jet impingement depends on the swirl angle obtained by swirling nozzles with helical inserts. In addition, introducing the swirl motion could improve the mixing characteristics via a broadening of the impingement region rather than heat transfer rates caused by the rapid decrease of the swirl intensity in the axial direction.

The jet fountain is an important factor affecting the heat transfer characteristics when multi-jet impingement is considered. Katti and Prabhu [15] experimentally investigated the effect of different span-wise pitches on the local heat transfer coefficient distribution on the plate by an array of multi-jet impingement. Their study showed that a span-wise pitch of 4 times diameter of hole performs better than that of 2 or 6 times, according to the analysis of the $\overline{Nu}$ and the pressure loss coefficient. San and Lai's research [16] showed that the *Nu* number is determined by H/d, S/d and Re. With a fixed H/d and Re, there is an S/d value corresponding to the optimal heat transfer performance. Gardon et al. [17, 18] found that the heat transfer effect at impingement stagnation point could be greatly improved when the nozzle-to-flat distance ranges from 5 to 7 times the diameter of nozzle. There will be a secondary peak phenomenon of *Nu* when the impingement distance of H/d is small, and the value is observed when H/d is primarily less than 3 and its location shifts towards the impingement stagnation point with the decrease of H/d [19].

In addition to the structure parameters, there are many studies on the effects of the flow factors. Considering the influence of impingement jet angle, Goldstein and Franchett [20] performed an experimental study of the heat transfer characteristics of an impinging jet on a flat surface, and the local heat transfer rates were reported as the inclined angles were changed from 30° to 90°. Lee and Lim [21] experimentally investigated the characteristics of heat transfer of the inclined impinging jet on a concave/convex surface by using the transient liquid crystal method; the *Nu* value at the stagnation point was confirmed to decrease as the tilt angle increases with a fixed *Re*. Heo et al. [22] found that the overall heat transfer increases with the pitch of the vertical jet nozzles, and the inclination angle of the staggered jet nozzles shows a peak value at approximately 60° when S/d equals 4. In addition, the flow parameters were found to have a significant effect on the multi-jet impingement heat transfer rates. Many studies showed that the local *Nu* number increases with the increase of the *Re* number, whether at a high [23] or low [24] Reynolds number, with the former having higher possibility to exhibit the second peak phenomenon of the local *Nu* number. Miao et al. [25] found that the hybrid cross-flow orientation causes higher local/averaged *Nu* numbers than both parallel and counter cross-flow orientations because the former creates fewer cross-flow effects and a smaller pressure drop.

Since the impinging surface in the bleeding air anti-icing system is a closed chamber, the experimental design will be more difficult. To the best knowledge of the authors, quite a few studies [26, 27] have used the multi-jet impingement on the airfoil with an array of round holes. Furthermore, the bleeding air anti-icing system consumes much energy from the jet engine [28], making it essential to increase the heat transfer rates to save onboard energy. Thus, the present work aims to investigate the heat transfer characteristics of the impinging jet on the leading edge of the wing, and the NACA0015 airfoil was selected as a case study. As the first part of a series of research works, the objective of the current work will focus on a combined numerical and experimental study to explore the heat transfer performance of sonic impingement jets on the concave surface.

2. Experiment apparatus and measurement procedure

Experiments were conducted in the anti-icing/de-icing research laboratory at Beihang University, China.

2.1. Experimental apparatus

Fig. 1 shows the experimental set up of the multiple impingement jet system. The experimental apparatus mainly includes four systems: A. test section; B. data acquisition system; C. motion control system; and D. the air supply system.

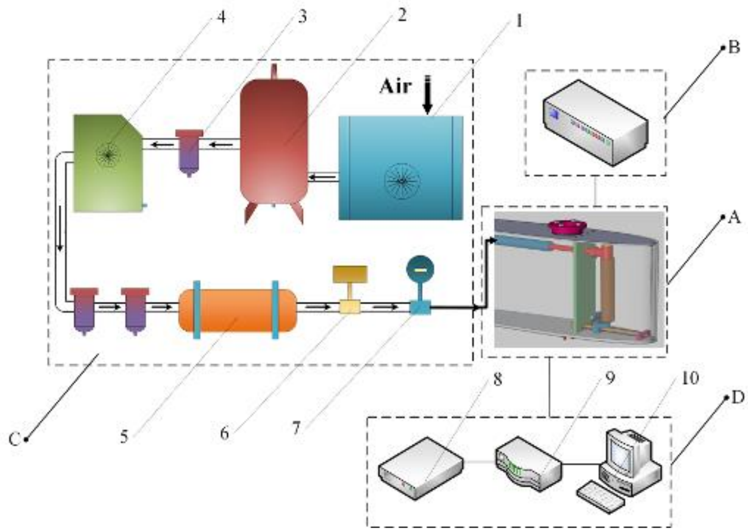

Fig. 1. Schematic of the experimental apparatus

A. test section; B. motion control system; C. the air supply system; D. data acquisition system;

1- air compressor; 2-air tank; 3-air filter; 4-refrigerant air drier; 5-heat exchanger; 6- electric regulating valve;

7- flow meter; 8-heating control device; 9-data acquisition device; 10-computer

In the current work, a highly curved concave impingement plate of NACA0015 profile is used as the test section. The chord length of the current model is 1 m, as shown in Fig. 2. No. 7075 aluminum is selected as the material of the plate. Three round jet holes are distributed in the tube in a straight line. The present work uses the steady state method to obtain the heat transfer coefficient according to Eqs. (3) to (8) in section 2.2. A T-type thermocouple is set in the T-type telescope tube that is close to jet holes to measure the temperature of the jet air T_j. Nineteen and nine K-type thermocouples with an outer diameter of 1 mm are set along the span and chord directions, respectively, in order to measure the temperature of the impingement wall T_w, as shown in Fig. 2. The thermocouples are placed in the blind-holes that drilled from outer wall surface of the profile with heat conduction glue. The distance from the thermocouples to the inner wall surface is 0.5 mm. The thermal conductivity of the aluminum is approximately 173 W/m.K. The thickness of the plate is 3 mm. Using one-dimensional steady heat conduction of Fourier transform, it is recognized that the difference of the temperature between inner and outer wall surface is less than 0.03 ^{o}C. Thus, the thermal resistance could be neglected. In the data acquisition system, an Agilent® 34972A acquisition instrument is used to record the experimental data, including the air temperature, the pressure and the mass flow. The accuracy of the thermocouples was within 0.5 ^{o}C. The air mass flow rate is measured using a vortex flow meter calibrated with an uncertainty of $\pm 5\%$. The accuracy of the pressure transducer is $\pm 0.25\%$ with the readings ranging from 0 to 0.8 MPa. To obtain the designed parameters, a motion control system (see Fig. 2) is designed to change different H/d and jets angles by using two linear motors and stepper motors, respectively. The PLC motion control device is composed of a DC power supply, a motor PLC controller, and two stepper motor drivers. In the air supply system, the air is provided by an air compressor, and the mass flow rate is controlled through an electric regulating valve. Before entering the test section, the air will be dried using a refrigerant air drier. To generate the sonic impinging jets, the air pipeline pressure is maintained at 0.4 MPa. The initial velocity and mass flow of each hole should be kept the same.

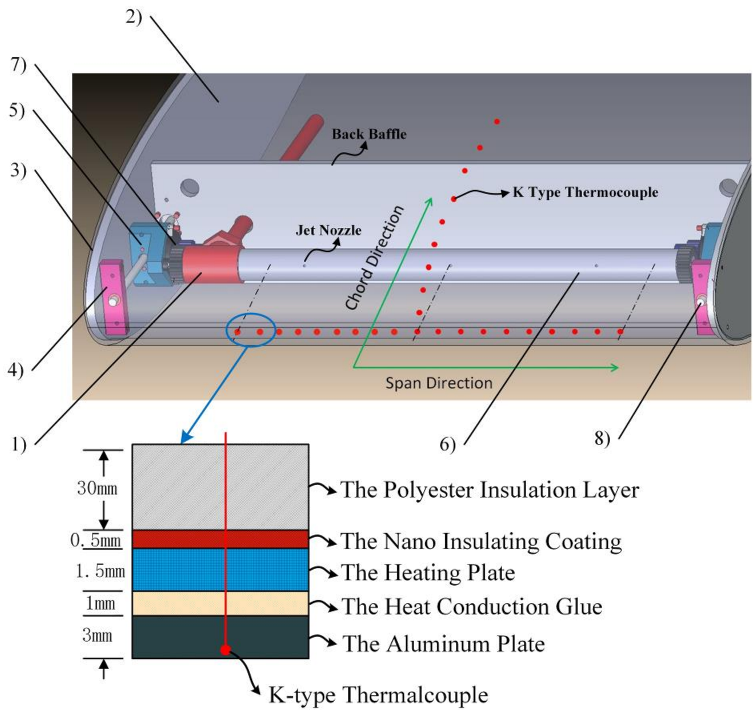

Fig. 2. Design diagram of the experiment element

1)-T-type telescope tube 2)-the baffle 3)- the impingement aluminum plate 4)- fixed end of linear motor 5)- the slider of ball-screw 6)- tube of impingement jets 7)-the stepper motor 8)- linear motor

For the purpose of simplification, the inverse heat flux method is adopted, in which all the outer surfaces are heated by an AC thin silica heating plate, and the internal air temperature is kept at the temperature of 10 °C through the heat exchanger in the refrigeration system. Two insulation layers are set to reduce the energy loss of the heating layers. A 0.5-mm RAYWAY® nanocoating (thermal conductivity: 0.0012 W/m^2·°C) is spread evenly onto the heating plate, and a 30-mm black polyester insulation layer (thermal conductivity is less than 0.034 W/m^2·°C) is glued onto the coating.

2.2. Uncertainty analysis

The uncertainties of the measurement in the experiment are dependent on the experimental conditions and the measurement instruments. The uncertainty method described by Holman [29] is used in the present study. The errors are individual components of the measurement error.

Therefore, the uncertainties of independent parameters are firstly computed, and consequently uncertainties of dependent parameters are calculated based on their relationship with independent parameters. The result R is a given function of the independent variables x_1, x_2, x_3, …x_n.

Thus,

$$R = R(x_1, x_2, x_3, ..., x_n) \tag{1}$$

The independent variables ofw_1, w_2, … ,w_3 are the uncertainties; thus, the uncertainty in the result w_R can be evaluated by:

$$w_R = \left[\left(\frac{\partial R}{\partial x_1} w_1 \right)^2 + \left(\frac{\partial R}{\partial x_2} w_2 \right)^2 + \cdots + \left(\frac{\partial R}{\partial x_n} w_n \right)^2 \right]^{1/2} \tag{2}$$

The local/averaged Nu number and heat transfer coefficient will be calculated according to Eqs. (3) to (8). The wall temperature T_w and jet air temperature T_f are measured during the experiment.

$$Nu = \frac{hd}{k} \tag{3}$$

$$\overline{Nu} = \frac{\sum_{i=1}^{n} Nu_i}{n} \tag{4}$$

$$h = \frac{q_{conv}}{T_w - T_f} \tag{5}$$

The heat transfer rate between the wall and the impingement jets q_{conv} is obtained as:

$$q_{conv} = q_{heat} - q_{loss} \tag{6}$$

$$q_{loss} = q_{rad} + q_{nat} \tag{7}$$

$$q_{heat} = \frac{V^2}{RA} \tag{8}$$

where q_{red} is the radiation losses, q_{nat} is the free convection, and the q_{loss} is found to be less than 4.2% according to reference [30]. The uncertainties of the heat transfer coefficients can be calculated using the following equations:

$$\frac{dh}{h}=\left[\left(\frac{dq_{conv}}{q_{conv}}\right)^2+\left(\frac{T_w}{T_w-T_f}\frac{dT_w}{T_w}\right)^2+\left(\frac{T_f}{T_w-T_f}\frac{dT_f}{T_f}\right)^2\right]^{1/2} \tag{9}$$

$$\frac{dq_{conv}}{q_{conv}}=\left[\left(\frac{q_{heat}}{q_{conv}}\frac{dq_{heat}}{q_{heat}}\right)^2+\left(\frac{q_{loss}}{q_{conv}}\frac{dq_{loss}}{q_{loss}}\right)^2\right]^{1/2} \tag{10}$$

$$\frac{dq_{heat}}{q_{heat}}=\left[\left(2\frac{dV}{V}\right)^2+\left(\frac{dR}{R}\right)^2+\left(\frac{dA}{A}\right)^2\right]^{1/2} \tag{11}$$

The calculation results show that the maximum uncertainty for the *Nu* number is less than $\pm 4.62\%$ in the repeatability test.

3. Computational details

3.1. Turbulence model

The turbulent flow pattern of the impingement multi-jets in the anti-icing system moves in complex irregular paths, causing stronger momentum and energy exchange between the fluid and solid wall. It is stated that the impingement multi-jets flow field could be divided into four regions; the details of the study can be found in a previous publication by Weigand and Spring [6] and will only be described briefly here for the sake of completeness. As is shown in Fig. 3, these four typical regions are: (1) the free jet region, (2) the impingement region, (3) the wall jet region and (4) the fountain flow region. In the free jet region, fluid exits from the holes into free space after entraining into the jets and then is accelerated. At the centerline, the fluid maintains its exit velocity while diffusing with the fluid from the shear layer. In the impingement region, the fluid flows toward the impingement wall while decelerating and changing its flow direction, as the core velocity decreases absolutely. In the jet stagnation point, the velocity of the fluid decreases to zero and accelerates quickly along the direction parallel to the wall. In the wall jet region, with the increasing radial distance from the stagnation point, compared with the stagnation point, the heat transfer characteristics between the wall and the impingement jet show noticeable differences. In the stagnation point region, the direction of the fluid flow is perpendicular to the impingement wall and parallel to the heat transfer direction between the wall and fluid. In the wall jet region, the flow field tends to be stable, and the heat is transferred mainly by the convection. In the fountain flow region, there are recirculating vortices formed via the shear layer expansion of the interactions between two jets.

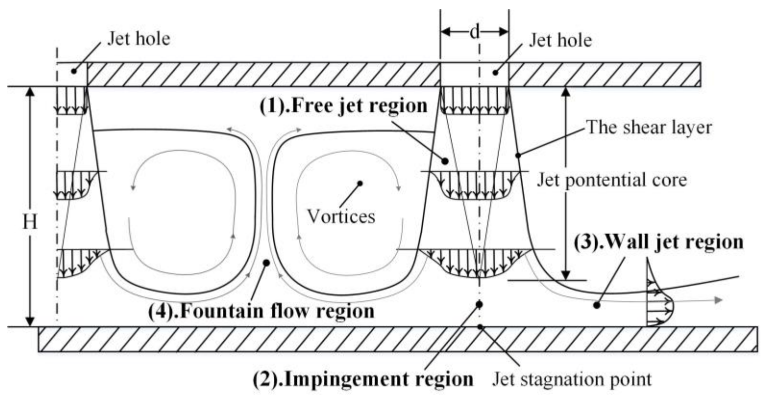

Fig. 3. Schematic illustration of the flow pattern of the impingement multi-jets.

3.2. Mesh analysis

The mesh density is carefully scaled in order to obtain high precision of numerical results since insufficient mesh would lead to serious computational error [31]. In addition, it is necessary to investigate the sensitivity of the number of grid nodes to the predicted results. Thus, the analysis of the effect of the near-wall cells size is performed to determine a suitable mesh [32]. The identified dimensionless parameter y^+, defined as in Eqs. (12) to (14), is the dimensionless distance from the wall for turbulent flows.

$$y^+ = \frac{y_p u^*}{\nu} \tag{12}$$

$$u^* = \sqrt{\frac{\tau_w}{\rho}} \tag{13}$$

$$\tau_w = \mu \frac{\partial U}{\partial y}\bigg|_{y=0} \tag{14}$$

Where y_p is the actual height of the first layer cell, and τ_ω is the wall shear stress.

It can be seen that eight different cell numbers and the corresponding $\overline{y^+}$ values (the average y^+ value along the wall) are investigated in this study. The calculation model of an impingement jet with a round hole on a semicircular surface is chosen. The computed results are compared with the experimental data of Choi et al. [33]. Fig. 4 indicates the significant influence of the cell numbers on the local *Nu* number distribution.

When $\overline{y^+} \leq 1$, there is a secondary peak phenomenon predicted in all of the meshes. However, when $\overline{y^+} > 1$, the secondary peak completely disappears. With the decrease of the $\overline{y^+}$ value, the computational results agree well with the experimental data. Considering both numerical accuracy and computing cost, the grid density of $\overline{y^+} = 1$ is chosen for all the cases in the current study.

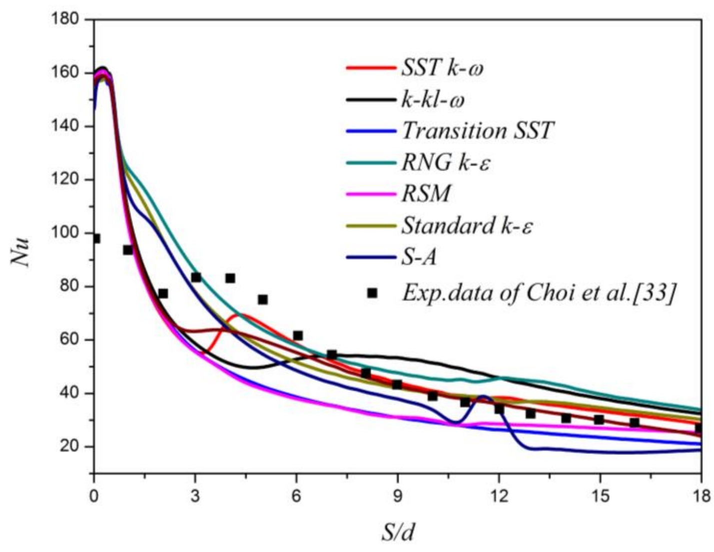

Fig. 4. Comparison of the local *Nu* number along the wall by eight $\overline{y^+}$ values with Choi et al. [33]

According to the constraints of $\overline{y^+} = 1$, the total mesh number of the computation model is approximately 1.6 million elements, as shown in Fig. 5. It should be noted that the mesh near the impingement hole is increased in order to improve the computational accuracy.

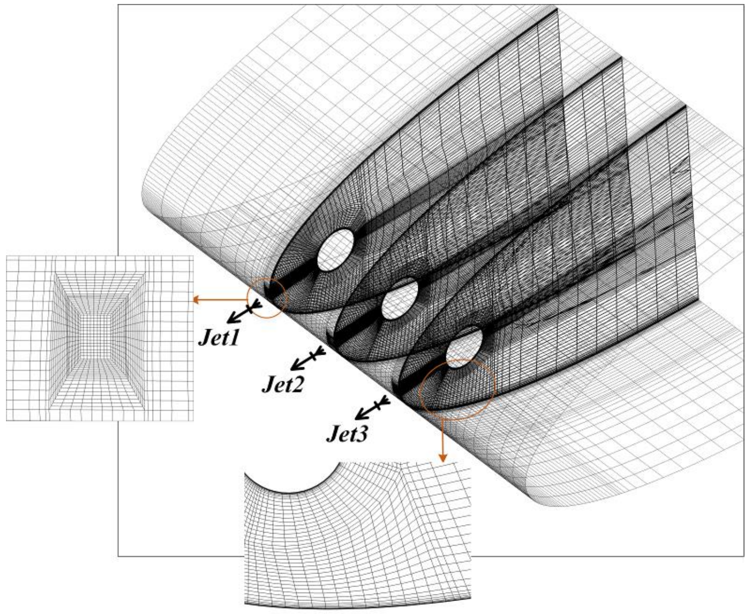

Fig. 5. The mesh for the computation

3.3. Boundary conditions and numerical setup

Fig. 6 shows the schematic of the boundary conditions. The outlet surfaces are set as the outflow condition. The other parts are set as a no-slip wall of adiabatic boundary conditions. The mass flow inlet boundary condition is set at each hole of the jets. The no-slip and constant heat flux value of 1500 W is set for the impingement concave surface. The pressure outlet boundary condition is used for the outlet, and it is a 3 mm round hole on the wall. In the numerical investigation, the CFD code FLUENT developed based on the finite volume technique is used. The basic equations are solved numerically by a coupled algorithm, which is a density-based solver in which the equations are solved simultaneously. The Courant number is set to 50, and the explicit-relaxation factors of momentum and pressure are both set to 0.9. During the computation, a steady-state calculation is conducted. Second order upwind scheme is used to discretize the pressure, momentum, turbulent kinetic energy and energy terms. Iterations are continued until the residual for all equations, such as the continuity and energy equation, based on the changes in the variables (i.e., pressure, velocity, temperature, etc.) between the current and previous iterations is $\frac{\left|v_{ic}-v_{ip}\right|}{v_{ip}}<10^{-3\ 5}$. The values of the parameters, such as flow temperature, range of H/d, S/d, jets inclination angle (θ) and diameter of hole (d), are listed in Table 1.

Table 1 The values of the parameters of *the* numerical calculation

Parameters	**Value**
Flow temperature	283.15 K
The heating flux	1500 W/m^2
Diameter of jets tube (D)	36 mm
Diameter of hole (d)	2~5 mm
H/d	10~30
S/d	20~35
Re	47367
Jets angle	0~30°

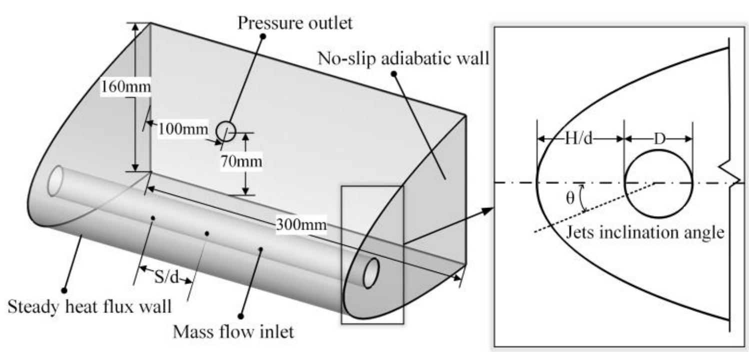

Fig. 6. The boundary conditions of the calculation domain

The *SST k-ω* model developed by Menter [34] is used to effectively blend the robust and accurate formulation in the near-wall region with the free stream independence of the *k-ω* model in the far field [35].

4. Results and analysis

4.1. Model validation

Prior to the aimed calculation, it is crucial to select a proper turbulence model. In the current work, eight extensively used RANS-based turbulence models, such as *RNG k-ε*、*Realizable k-ε*、*S-A*、*Standard k-ω* and *SST k-ω*, are demonstrated and compared with the open published experimental data in Choi et al. [33] for validation.

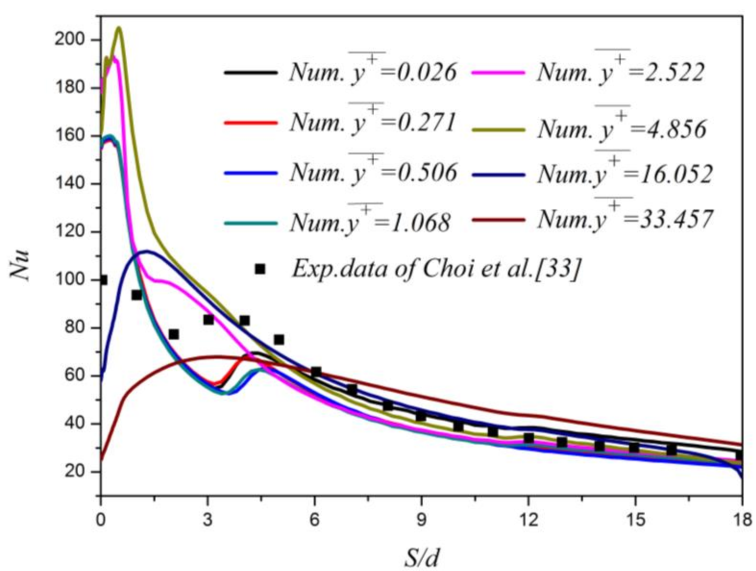

Fig. 7. Comparison of local *Nu* number of different turbulence models with Choi et al. [33]

It is found from Fig. 7 that only the *SST k-ω* model predicts the secondary peaks of local *Nu* number successfully, which occurs at small H/d. The *SST k-ω* model is a superposition of the *k-ω* model with the *k-ε* model. While the *k-ε* model is used for the fully turbulent region, the model changes at the entrance of the boundary layer and behaves like the *k-ω* model. In addition, the formulation of the turbulent viscosity is changed to take into account transport effects in the turbulent main stresses [36]. Finally, the *SST k-ω* turbulence model is selected in the present study. The computed results are in good agreement with the results of Hofmann et al. [37] due to its comparatively low computational costs and great performance.

4.2. Heat transfer characteristics of the multi-jet impingement

4.2.1. Effect of H/d ratio

To investigate the influence of the H/d (non-dimensional distance between the jet holes exit and the concave surface) ratio, both experimental and numerical studies are conducted. The H/d values of 10, 15, 20 and 25 are considered, which are commonly used in the bleeding air anti-icing system. The comparison results of the experimental and numerical local *Nu* number for different H/d ratios are shown in Fig. 8. The maximum *Nu* number appears at the stagnation point of jet 2, while decreases with increasing radial distance. It is known that convection is a phenomenon of heat transfer by the movement between fluid and solid, and the thermal resistance mainly depends on the thickness of viscous boundary layer. The boundary layer thickness of the impinging multi-jet will be the thinnest at the stagnation point, which is approximately one-hundredth of the jet hole diameter according to the analytical solution of [38]. The thermal resistance reaches the minimum, which achieves strong heat transfer capacity. As a consequence, the flow accelerates from zero and reaches the maximum value at 1-2 hole diameter distance from the stagnation point [39] at wall jet region. With the increase of the H/d ratio, the shear layer widens before impacting on the wall. The kinetic energy is dissipated gradually with the expansion of the jet shear layer, which causes the local *Nu* number value decreases directly. The interference between jets before impingement is quite obvious, which results in the *Nu* number at the stagnation point of jet 2 larger than the other two. The same trend was also observed in San et al.'s study [16]. The numerical results of the flow streamlines are shown in Fig. 9; these results were primarily obtained to analyze the flow pattern over the concave surface. As the H/d increases, the size of the fountain region becomes larger, which is a clear demonstration that the change of H/d ratio has a significant effect on the fountain zone around the stagnation point. The core width decreases gradually with the increasing distance from the holes, and the jet potential core disappears after nearly five holes diameters from the jet exit [40].

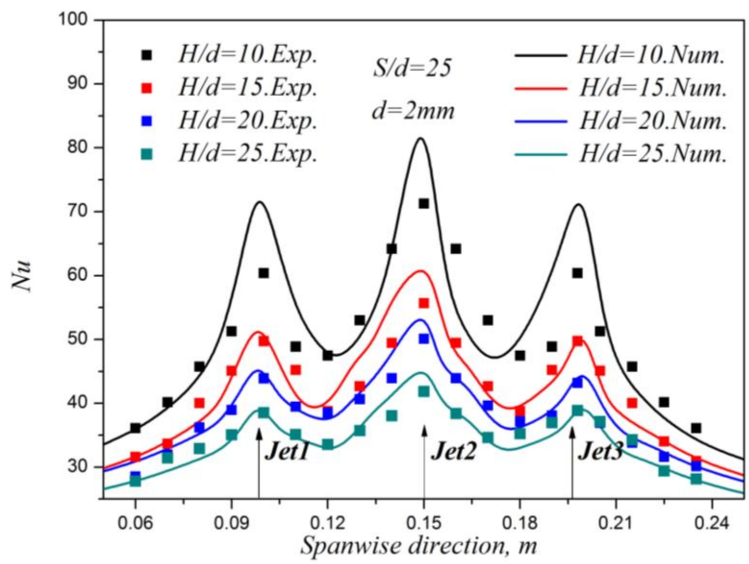

Fig. 8. Comparison of the experimental and numerical local *Nu* number results for different H/d ratios

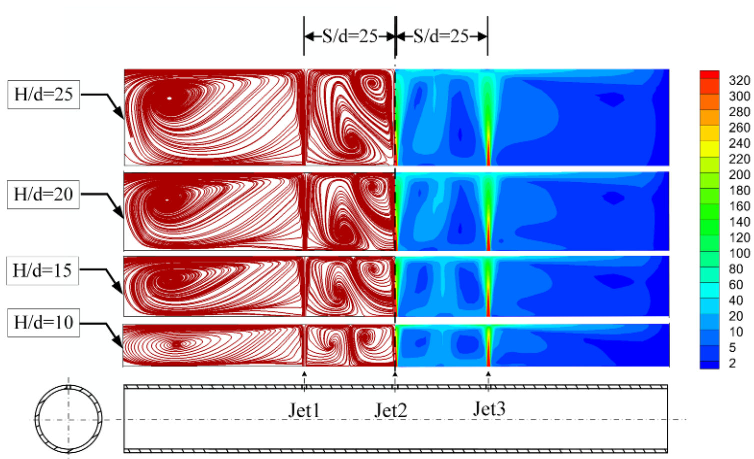

Fig. 9. Flow pattern with different H/d ratio along the span-wise direction

Fig. 10 presents the profiles of experimental and numerical local *Nu* number at the stagnation point for nine different H/d values ranging from 10 to 30, with S/d and d fixed. It is found that the distribution of the local *Nu* number of jet 2 agrees well with the experimental results. The maximum difference is 8.31%, which is an acceptable value.

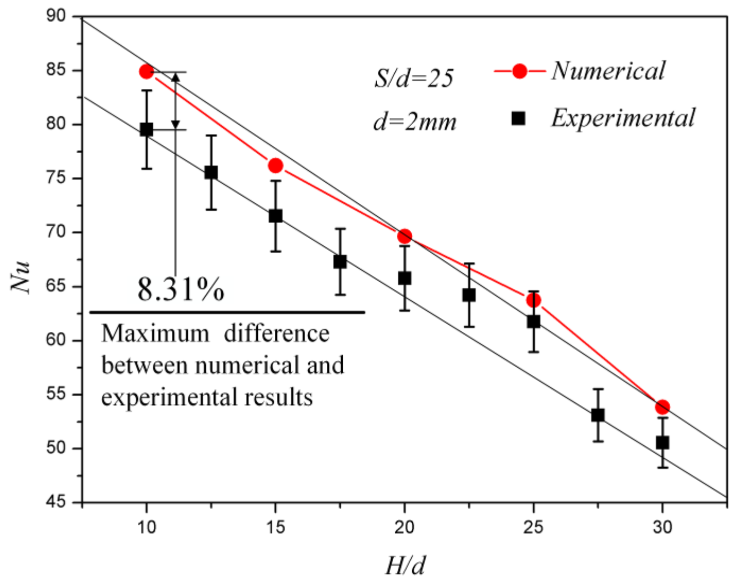

Fig. 10. Comparison between numerical and experimental results of the *Nu* number at the stagnation point of jet 2

4.2.2. Effect of the diameter of the hole

A sonic jet is used to ensure that the velocity and mass flow of each hole's exit is consistent. The jets mass flow increases as the diameter of the holes becomes larger, as shown in Figs. (11) and (12). Both the experimental and simulation results show that, with the increase of the diameter of the holes, the *Nu* number value increases sharply. The $\overline{Nu}$ of d = 5 mm is almost eight times as much as the value of d = 2 mm. Nevertheless, the consumed air mass flow is also increased by nearly seven times. Since too much bleeding air from the engine will reduce the thrust seriously, the method of enlarging the diameters of the jets holes in the anti-icing system of aircraft to improve the heat transfer efficiency is not appropriate.

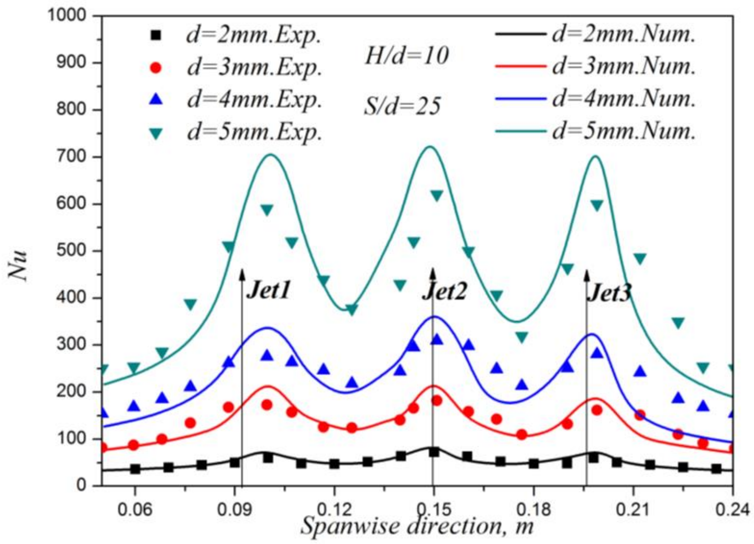

Fig. 11. Comparison of the experimental and numerical local *Nu* number results for different diameters of holes

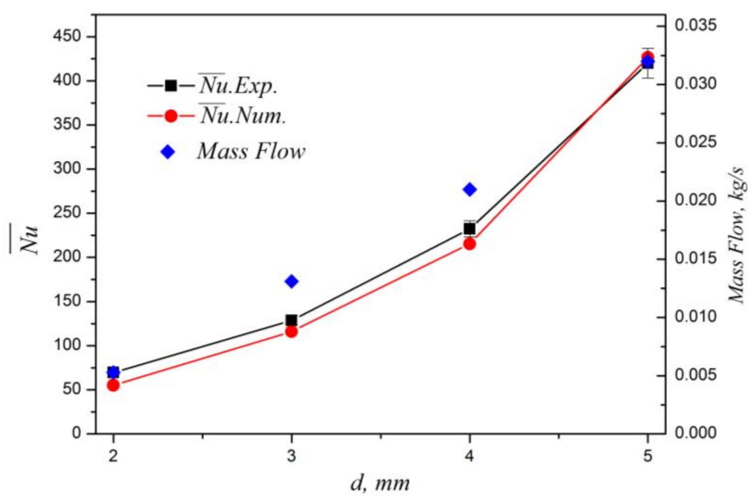

Fig. 12. Comparison of the $\overline{Nu}$ for different holes diameters

4.2.3. Effect of the S/d ratio

The effect of S/d on the local distribution of *Nu* number and flow streamlines can be studied in Figs. (13) and (14), with H/d=10 and d=2 mm. It can be found that the jet 2 peak value of *Nu* number at S/d=20 is larger than the other cases. Since the narrower distance can cause more limitations of the dissipation from the shear layer before impacting on the stagnation point, which leads to the concentration of the jet core potential energy. With the decrease of S/d, the vortices size between jets becomes narrower, as shown in Fig. 14. The flow channel is downsized, and the heat transfer performance of fountain flow region is improved. Fig. 15 shows the effect of S/d on the variation of the $\overline{Nu}$ of impingement surface for various H/d. For S/d=20, 25, 30 and 35, the distribution of $\overline{Nu}$ has the same trend: the heat transfer efficiency decreases with the increase of H/d ratio. $\overline{Nu}$ at S=30 d performs better than 20 d, 25 d and 35 d because, as S/d decreases, the heat transfer capacity increases in jet 2 but decreases in jet 1, jet 3, and the wall jet region. However, when S/d becomes too high, the interaction between the jets is weakened.

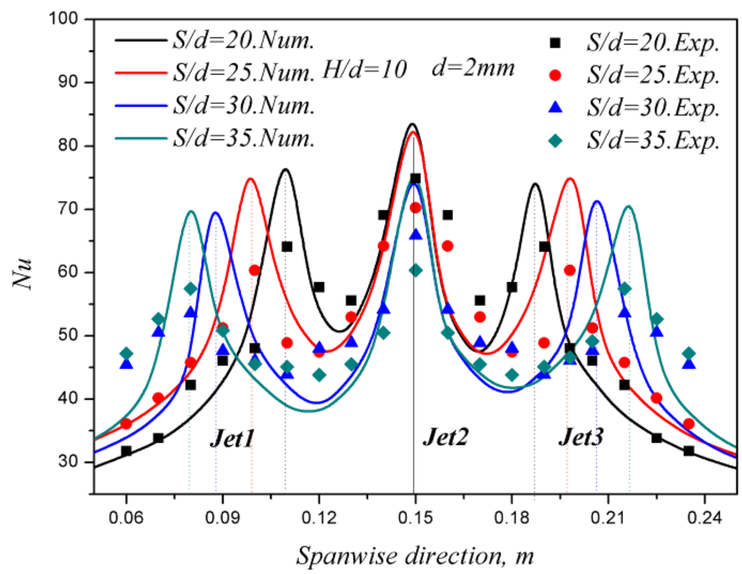

Fig. 13. Comparison of the experimental and numerical local *Nu* number results for different S/d ratios

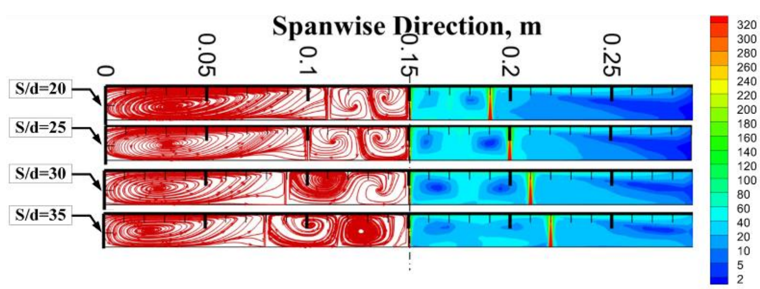

Fig. 14. Streamlines display for different S/d ratios

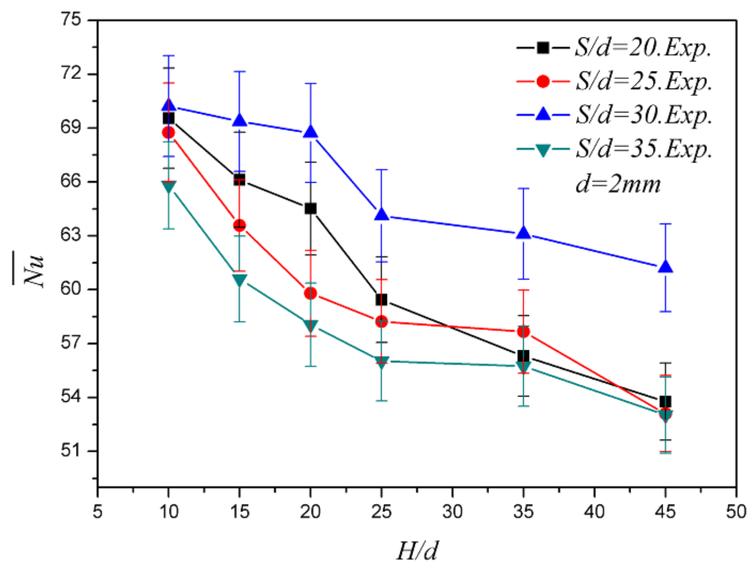

Fig. 15. Effect of S/d on the variation of the $\overline{Nu}$ of impingement surface for various H/d values

4.2.4. Influence of the jet angles

The influence of different jet angles on the heat transfer capacity and flow pattern along the chord-wise direction of concave surface is numerically studied; the results are shown in Figs. (16) to (18). Fig. 16 shows the effect of the local *Nu* number around the stagnation point of jet 2 along the chord-wise direction with respect to the inclined angle. It is indicated that with the increase of the jets inclination angle, the *Nu* number at the stagnation point gradually increases, and the location with maximum *Nu* becomes further from the origin. A possible reason for this result is as follows. The impingement target is the leading edge of NACA0015 airfoil with high curvature surface. With the increase of the inclined angle, the distance between the jet exit holes and the stagnation point decreases. According to the results above, the *Nu* number at the stagnation point increases over a certain range. Fig. 17 shows the variation of $\overline{Nu}$ and Nu_{max} with respect to the jet inclination angle. It can be observed directly from this figure that the maximum $\overline{Nu}$ value occurs at the inclined angle of 15°. Fig. 18 shows the flow patterns at different jet inclination angles. The flow situation with inclined angle of 15° is found to be the most complex because the most vortices are present, resulting in the strongest disturbance for the viscous sub layer and, thus, the strongest heat transfer capacity. Therefore, it is significant to improve the heat transfer efficiency of the curved surface by adjusting the inclined angle of the jets.

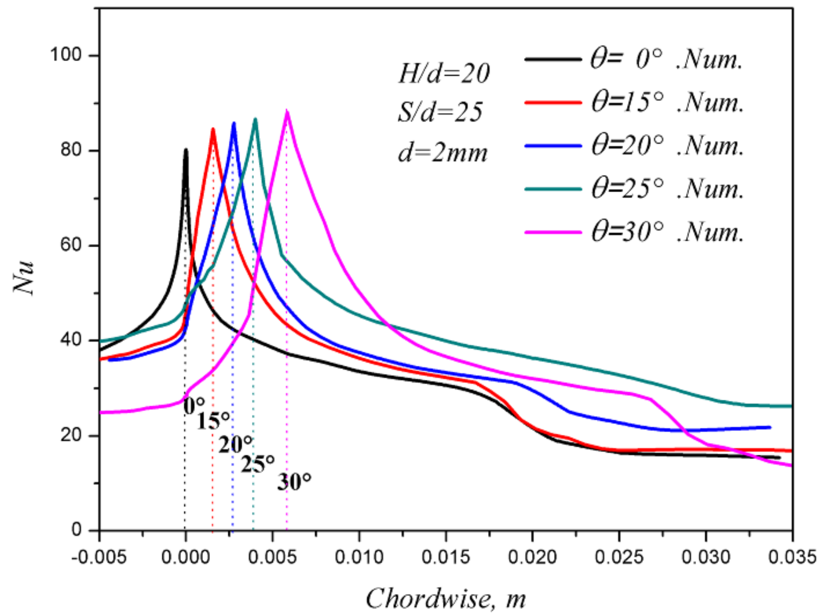

Fig. 16. Effect of the local *Nu* number around the stagnation point of jet 2 along the chord-wise direction with respect to the inclined angle

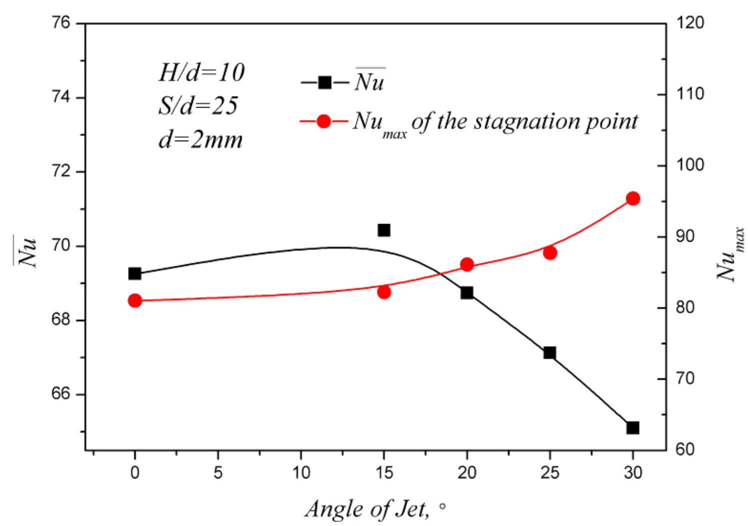

Fig. 17. Variation of the average/max *Nu* number with respect to the jet inclination angle

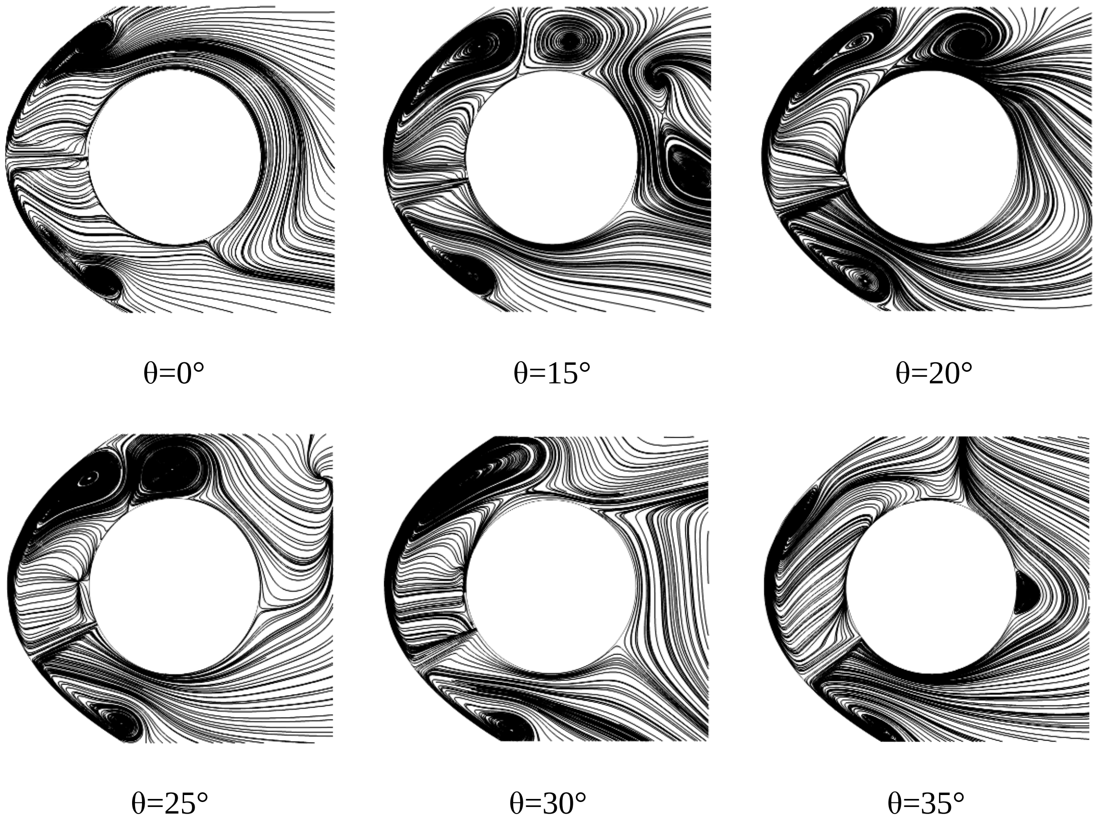

Fig. 18. Flow patterns for different jets inclination angles

5. Conclusions

A combined experimental and numerical study was conducted to investigate the multi-jet impingement from round holes to a NACA0015 airfoil concave surface. The appropriateness of turbulence model and mesh were verified. Various structural parameters were performed to analyze the distribution of $Nu/\overline{Nu}$ number, in which the H/d is varied from 10 to 25, S/d is varied from 20 to 35, d is varied from 2 to 5 mm, and θ is varied from 0 to 30°. Furthermore, streamline diagrams were presented to understand the heat transfer results, such as the fountain flow, and the primary vortices structure near the stagnation point. Analysis of the experimental and numerical results may lead to the following main conclusions:

- With the increase of H/d, the distribution of the local *Nu* number on the impingement wall decreases gradually at all the radial locations. The maximum $\overline{Nu}$ values appeared at H/D=10 in the present study.

- With the hole diameter increases from 2 mm to 5 mm, the heat transfer capacity of multi-jet impingement would be improved greatly, by nearly 7 times. Accordingly, the mass flow increases nearly seven times. Hence, it is not appropriate to improve the heat transfer efficiency only by enlarging the diameters of the jet holes in the anti-icing system of aircraft.
- The distance between adjacent holes, at S = 30 d, performs best on the basis of the $\overline{Nu}$ compared with the 20 d, 25 d and 35 d due to the higher interaction between jets. Therefore, the S/d ratio can be one of the significant factors for the fluid flow of impingement multi-jets.
- Due to high curvature of the leading edge of the concave surface in the present study, the *Nu* value at the stagnation point increases as inclination angle changes from 0° to 30°. Analytical results based on the flow pattern in the vicinity of the stagnation point confirms these trends.

Acknowledgements

The research work is funded by the National Basic Research Program of China (973 program) grant No. 2015CB755803.

References

[1] P. Planquart, G. V. Borre, J.M. Buchlin, Experimental and numerical optimization of a wing leading edge hot air anti-icing system.AIAA-paper. (2005).

[2] F. Saeed, Numerical simulation of surface heat transfer from an array of hot-air jets. J. Aircr. 45(2008)700-714.

[3] J. Han, S. Ekkad, Recent development in turbine blade film cooling. Int. J. Rotating Mach. 7(2001)21-40.

[4] M. Anwarullah, V. V. Rao, K. V. Sharma, Experimental investigation for enhancement of heat transfer from cooling of electronic components by circular air jet impingement. Heat Mass Transfer. 48(2012)1627–1635.

[5] B. Weigand, S. Spring, Multiple jet impingement-a review. Int. Symp. on Heat Transfer in Gas Turbine Systems 9*14 August 2009, Antalya, Turkey.

[6] B. Weigand, S. Spring, Multiple jet impingement-a review. Heat Transfer Research. 42(2011).

[7] A. C. Chambers, D. R. H. Gillespie, T. Peter. Ireland, R. Kingston, Enhancement of pingement cooling in a high cross flow channel using shaped impingement cooling holes. J. Turbomach. 132(2010)995-1004.

[8] M. A. R. Sharif, N. M. Ramirez, Surface roughness effects on the heat transfer due to turbulent round jet impingement on convex hemispherical surfaces. Appl. Therm. Eng. 51 (2013) 1026-1037.

[9] C. Wan, Y. Rao, P. Chen, Numerical predictions of jet impingement heat transfer on square pin-fin roughened plates. Appl. Therm. Eng. 80 (2015) 301-309.

[10] M. M. Rahman, C. F. Hernandez, J. C. Lallave, Free liquid jet impingement from a slot nozzle to a curved plate. Numer. Heat Transfer, Part A 57(2010)799–821.

[11] J. Lee, S. Lee, The effect of nozzle configuration on stagnation region heat transfer enhancement of axisymmetric jet impingement. Int. J. Heat Mass Transfer. 43 (2000) 3497-3509.

[12] L. A. Brignoni, S. V. Garimella, Effects of nozzle-inlet chamfering on pressure drop and heat transfer in confined air jet impingement. Int. J. Heat Mass Transfer. 43 (2000) 1133-1139.

[13] A. Ianiro, G. Cardone, Heat transfer rate and uniformity in multichannel swirling impinging jets Appl. Therm. Eng. 49 (2012) 89-98.

[14] M. Wannassi, F. Monnoyer, Fluid flow and convective heat transfer of combined swirling and straight impinging jet arrays. Appl. Therm. Eng. 78 (2015) 62-73.

[15] V. V. Katti and S. V. Prabhu, Influence of spanwise pitch on local heat transfer for multiple jets with crossflow. J. Thermophys Heat Transfer. 22(2008)654-668.

[16] J. San, M. Lai, Optimun jet-to-jet spacing of heat transfer for staggered arrays of impinging air jets.Int. J. Heat Mass Transfer. 44(2001) 3997-4007.

[17] R. Gardon, J. Cobonpue, Heat transfer between a flat plate and jets of air impinging on it. International Heat Transfer Conference, Pt. 2. (1961)454-460.

[18] R. Gardon, J. C. Akfirat, The role of turbulence in determining the heat transfer characteristics of jet impingings. Int. J. Heat Mass Transfer. 8(1965)1261-1272.

[19] V. Katti, S.V. Prabhu, Experimental study and theoretical analysis of local heat transfer distribution between smooth flat surface and impinging air jet from a circular straight pipe nozzle. Int. J. Heat Mass Transfer. 51(2008)4480-4495.

[20] R. J. Goldstein, M. E. Franchett, Heat transfer from a flat surface to anoblique impinging jet. Int. J. Heat Transfer. 110(1998)84-90.

[21] C. Lee and K. Lim, Heat transfer characteristics of turbulent impinging jet in impingement angle and curved surface configuration using transient liquid crystal method. J. Therm. Sci. Technol. 2(2007)224-235.

[22] M. Heo, K. Lee, K. Kim, Parametric study and optimization of staggered inclined impinging jets on a concave surface for heat transfer augmentation. Numer. Heat Transfer, Part A 61(2012)442–462.
[23] E. Baydar, Y. Ozmen, An experimental and numerical investigation on a confined impinging air jet at high Reynolds numbers. Appl. Therm. Eng. 25 (2005) 409–421.
[24] V. A. Chiriac, A. Ortega, A numerical study of the unsteady flow and heat transfer in a transitional confined slot jet impinging on an isothermal surface. Int. J. Heat Mass Transfer. 45 (2002) 1237-1248.
[25] J. Miao, C. Wu, P. Chen, Numerical investigation of confined multiple-jet impingement cooling over a flat plate at different crossflow orientaions. Numer. Heat Transfer, Part A 55(2009)1019-1050.
[26] M. Papadakis, Parametric investigation of a bleed air ice protection system 44th AIAA aerospace Sciences meeting and exhibit 9-12, Reno, Nevada AIAA. (2006)1013.
[27] F. Saeed and I. Paraschivoiu, Optimization of a hot-air anti-icing system. 41th Aerospace Sciences Meeting & Exhibit. Reno, 2003.
[28] S. M. Jones, M. S. Reveley, J. K. Evans, F. A. Barrientos, Subsonic aircraft safety icing study. NASA, Tm. (2008)215107.
[29] J. P. Holman, Experimental methods for engineers. 8th ed, McGraw-Hill. New York. (2012).
[30] S. Caliskan, S. Baskaya, T. Calisir, Experimental and numerical investigation of geometry effects on multiple impinging air jets, Int. J. Heat Mass Transfer, 75(2014):685-703.
[31] M. Wolfshtein, Some comments on turbulence modeling, Int. J. Heat Mass Transfer 52(2009): 4103–4107.

[32] D. N. Sorensen, P. V. Nielsen, Quality control of computational fluid dynamics in indoor environments, Indoor Air. 13(2003)2-17.

[33] M. Choi, H. Yoo, G. Yang, J. Lee, D. Sohn, Measurements of impinging jet flow and heat transfer on a semi-circular concave surface. Int. J. Heat Mass Transfer 43 (2000) 1811-1822.

[34] F. R. Menter, Two-equation eddy-viscosity turbulence models for Engineering Applications. AIAA J. 32(1994)1598-1605.

[35] Fluent Inc. Fluent user's guide. (2006).

[36] D. C. Wilcox, Turbulence modeling for CFD, DCW Industries, LaCanada, CA. (2000).

[37] H. M. Hofmann, R. Kiser, M. Kind, H. Martin, Calculations of steady and pulsating impinging jets-an assessment of 13 widely used turbulence models. Numer. Heat Transfer, Part B 51(2007)565-583.

[38] B. Weigand, S. Spring, Multiple jet impingement-A Review. Heat Transfer Research. 42(2011)101-142.

[39] G. Abramovich, The theory of turbulent jets, MIT Press, Cambridge, Massachusetts, USA, 1963.

[40] H. Martin, Heat and mass transfer between impinging gas jets and solid surfaces, Adv. Heat Transfer. 13(1977)1-60.

Table and Figure Captions:

Table 1- The values of the parameters of the numerical calculation

Figure 1- Schematic of experimental apparatus: A. test section; B. motion control system; C. the air supply system; D. data acquisition system; 1-air compressor; 2-air tank; 3-air filter; 4-refrigerant air drier; 5-heat exchanger; 6- electric regulating valve; 7- flowmeter; 8-heating control device; 9-data acquisition device; 10-computer

Figure 2- Design diagram of the experiment element: 1-T-type telescope tube; 2-the baffle; 3- the impingement aluminium plate; 4- fixed end of linear motor; 5- the slider of ball-screw; 6- tube of impingement jets; 7-the stepper motor 8- linear motor.

Figure 3- Schematic illustration of the flow pattern of the impingement multi-jets.

Figure 4- Comparison of the local Nu number along the wall by eight $\overline{y^+}$ values with Choi et al. [32].

Figure 5- The mesh for the computation.

Figure 6- The boundary conditions of the calculation domain.

Figure 7- Comparison of local Nu number of different turbulence models with Choi et al. [32]

Figure 8- Comparison of the experimental and numerical local Nu number results for different H/d ratios

Figure 9- Flow pattern with different H/d ratio along the span-wise direction.

Figure 10- Comparison between numerical and experimental results of the Nu number at the stagnation point of jet 2

Figure 11- Comparison of the experimental and numerical local Nu number results for different diameters of holes

Figure 12- Comparison of the $\overline{Nu}$ for different holes diameters

Figure 13- Comparison of the experimental and numerical local Nu number results for different S/d ratios.

Figure 14- Streamlines display for different S/d ratios.

Figure 15- Effect of S/d on the variation of the $\overline{Nu}$ of impingement surface for various H/d values.

Figure 16- Effect of the local Nu number around the stagnation point of jet 2 along the chord-wise direction with respect to the inclined angle.

Figure 17- Variation of the average/max Nu number with respect to the jet inclination angle.

Figure 18- Flow patterns for different jets inclination angles.